

RESEARCH ARTICLE

Single cell force profiling of human myofibroblasts reveals a biophysical spectrum of cell states

Thomas B. Layton¹, Lynn Williams¹, Huw Colin-York², Fiona E. McCann¹, Marisa Cabrita¹, Marc Feldmann¹, Cameron Brown³, Weilin Xie⁴, Marco Fritzsche^{1,2}, Dominic Furniss³ and Jagdeep Nanchahal^{1,*}

ABSTRACT

Mechanical force is a fundamental regulator of cell phenotype. Myofibroblasts are central mediators of fibrosis, a major unmet clinical need characterised by the deposition of excessive matrix proteins. Traction forces of myofibroblasts play a key role in remodelling the matrix and modulate the activities of embedded stromal cells. Here, we employ a combination of unsupervised computational analysis, cytoskeletal profiling and single cell traction force microscopy as a functional readout to uncover how the complex spatiotemporal dynamics and mechanics of living human myofibroblast shape sub-cellular profiling of traction forces in fibrosis. We resolve distinct biophysical communities of myofibroblasts, and our results provide a new paradigm for studying functional heterogeneity in human stromal cells.

KEY WORDS: Focal adhesion, Myofibroblast, Single cell, Traction force

INTRODUCTION

Analysis of single-cell biology has illuminated crucial biological processes in health and multiple diseases (Giustacchini et al., 2017; Kinchen et al., 2018). These techniques quantify surrogate markers, such as mRNA molecules or protein abundance and subsequently ascribe functions to discrete cell types (Villani et al., 2017; Aizarani et al., 2019). However, pertinent to all fibrotic diseases, the functional characterisation of primary human stromal cells remains incomplete.

Myofibroblasts are crucial mediators of normal wound healing and contribute excessive extracellular matrix (ECM) during fibrosis (van Beuge et al., 2016; Wynn and Ramalingam, 2012). A central function of myofibroblasts is the generation of traction force, which plays a key role in remodelling the matrix and also modulates the activities of the embedded stromal cells (Liu et al., 2015; Hinz and

Gabbiani, 2003; Goffin et al., 2006). Despite several studies quantifying fibroblast traction force (Marinković et al., 2012; Rayan et al., 1996), we still lack an understanding of this process in human myofibroblasts (Wang et al., 2003). Indeed, we are yet to obtain precise force measurements in myofibroblasts that would enhance our understanding of their function (Hinz et al., 2001). At present, we are limited to force measurements of groups of cells without a single-cell perspective. In addition, we do not know whether distinct myofibroblast populations exist based on their biophysical characteristics. Single-cell force measurements would address these questions and allow the determination of functional heterogeneity in primary human myofibroblasts.

Although techniques such as culture force monitoring and collagen populated lattice modelling have elucidated critical regulatory processes of stromal cell contraction (Tseng et al., 2011; Polacheck and Chen, 2016), they report measurements of representative groups of cells and lack the required resolution to interrogate single-cell force profiles. Several techniques have been developed to measure force generation in individual cells and one that has gained prominence is traction force microscopy (TFM) (Colin-York et al., 2019a,b, 2016, 2017). TFM is based on the reconstruction of forces from a measured displacement field and uses hydrogels of defined stiffness with fiducial markers to track substrate deformations (Colin-York et al., 2017). Importantly, TFM allows for traction forces to be quantified at sub-cellular resolution (~1–2 μm), enabling distinct biophysical structures within cells to be studied. Hence, we hypothesised that TFM could be used to characterise the biophysical properties of human myofibroblasts.

Dupuytren's disease (DD) is a localised fibrotic condition of the hand and commonly treated by excision of the diseased fibrotic cords and associated myofibroblast-rich nodules (Verjee et al., 2009, 2010, 2013). Therefore, DD provides an ideal model disease to study human myofibroblasts. Here, we first defined the *in vivo* tissue mechanics in fibrosis and subsequently probed primary human myofibroblasts in a comparable mechanical environment. We uncovered distinct biophysical profiles of myofibroblast force generation and diverse cytoskeletal topologies which were modulated during cell spreading. Crucially, we provide the first evidence for distinct myofibroblast subpopulations with unique force profiles and characterise the mechanics of myofibroblast collagen interaction at subcellular resolution, which has important implications for understanding the functional roles of myofibroblasts in human fibrosis.


RESULTS AND DISCUSSION

Mapping the mechanical landscape in human fibrosis

The mechanical environment directly modulates stromal cell function and force measurements. Therefore, we first sought to define the native tissue mechanics of the myofibroblast-rich DD nodules. To quantify the Young's modulus (E) of nodules, we

¹The Kennedy Institute of Rheumatology, Nuffield Department of Orthopaedics, Rheumatology and Musculoskeletal Sciences, University of Oxford, Oxford OX3 7FY, UK. ²MRC Human Immunology Unit, Weatherall Institute of Molecular Medicine, University of Oxford, Headley Way, Oxford OX3 9DS, UK. ³Botnar Research Centre, Nuffield Department of Orthopaedics, Rheumatology and Musculoskeletal Sciences, University of Oxford, Oxford OX3 7LD, UK. ⁴Department of Inflammation Research, Celgene Corporation, San Diego, CA 92121, USA.

*Author for correspondence (jagdeep.nanchahal@kennedy.ox.ac.uk)

 T.B.L., 0000-0003-1934-7234; H.C.-Y., 0000-0002-6585-3237; F.E.M., 0000-0001-8151-8781; M.C., 0000-0002-8542-8967; M.F., 0000-0003-0800-7840; W.X., 0000-0001-8432-1853; M.F., 0000-0002-8712-7471; D.F., 0000-0003-2780-7173; J.N., 0000-0002-9579-9411

This is an Open Access article distributed under the terms of the Creative Commons Attribution License (<https://creativecommons.org/licenses/by/4.0/>), which permits unrestricted use, distribution and reproduction in any medium provided that the original work is properly attributed.

performed nano-indentation using atomic force microscopy (AFM) (Fig. 1A–C). The AFM cantilever was equipped with a 5 μm sphere-tipped probe, allowing measurements to be taken at cell-relevant scales. We observed a large range of nano-indentation

measurements across individual nodules (Fig. 1D), suggesting that the structure was relatively heterogeneous. The nodules had a Young's modulus of 9 kPa (± 5 kPa SEM) (Fig. 1D,E), comparable to values reported for other fibrotic tissues that range from

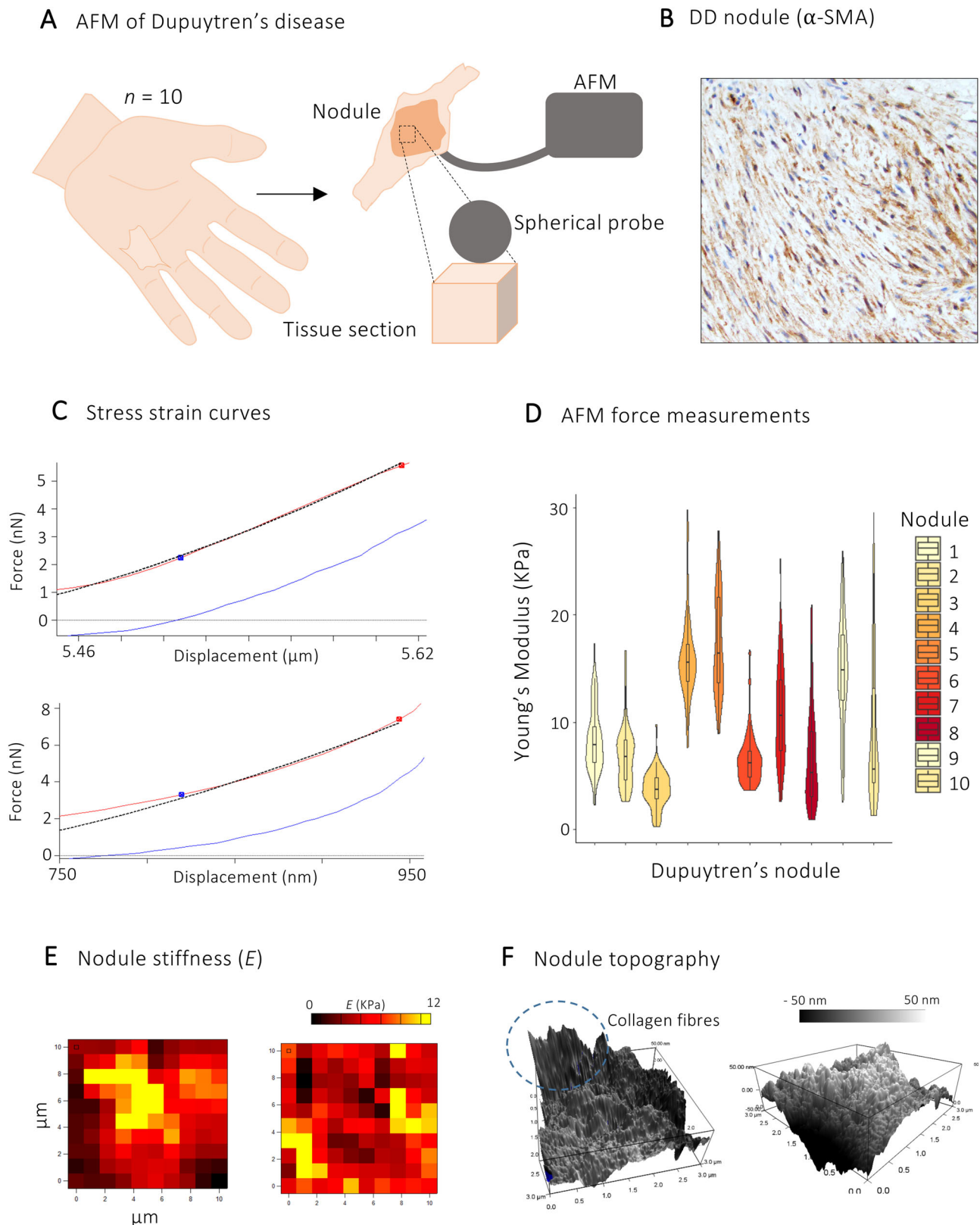


Fig. 1. See next page for legend.

Fig. 1. Mapping the mechanical landscape in human fibrosis.

(A) Schematic demonstrating experimental workflow for measurements of tissue stiffness. Central nodular tissue was dissected to cube-like structures and these were then sectioned in 30 μm slices. Tissue slices were probed using micro-indentation with a 5 μm sphere-tip probe mounted on the AFM cantilever. (B) Immunohistochemistry slide of DD nodule showing α -SMA staining. (C) Stress strain curves of AFM protocols for the application of mechanical force and measurements of two separate Dupuytren's nodules. (D) Violin plot showing Young's modulus of ten Dupuytren's nodules. Each point represents one micro-indentation measurement ($n=300$ per nodule). (E) Exemplar mechanical maps obtained by atomic force microscopy. Each map was derived from an independent DD patient nodule and provides a 100-point profile of Young's modulus (colour bar is inset). (F) Surface profiles showing topography of Dupuytren's nodules with linear structures of collagen fibres. Bounding box heights scaled at 100 nm.

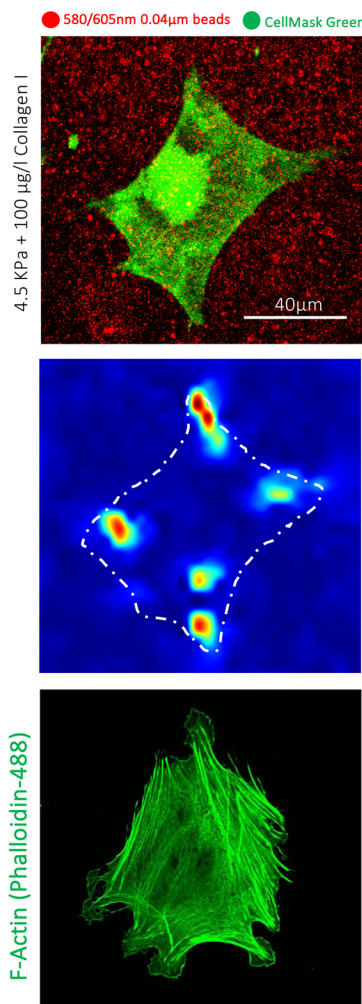
~ 10 – 20 kPa (Liu and Tschumperlin, 2011; Karki and Birukova, 2018; Liu et al., 2016, 2015).

Next, we explored the topography of DD nodules using high resolution AFM surface scans. In accordance with the stiffness measurements, the structure of the DD nodule was heterogeneous, with readily identifiable collagen bundles in a linear arrangement (Fig. 1F). The collagen bundles were present in an organised pattern that correlates with previous histological descriptions of nodules (Badalamente et al., 1983).

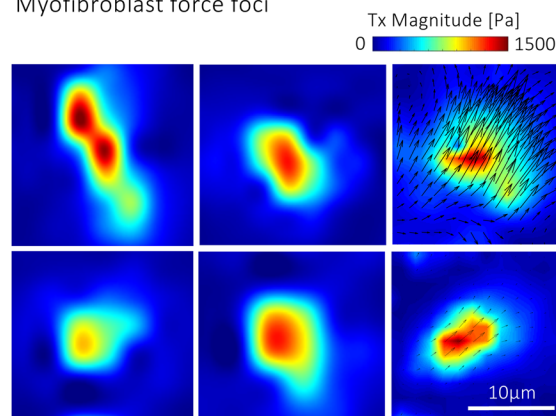
Characterising the biophysical profile of myofibroblast force foci

After defining the native tissue stiffness of DD nodules, we performed traction force microscopy on gels with a Young's modulus ranging from 0.5 kPa to 20 kPa. Cells were seeded on gels coated with type I collagen as this represents the most abundant ECM protein in nodules. We found that cells seeded on hydrogels with a Young's modulus of 4.5 kPa allowed reproducible quantification of bead displacements whilst lying within the range of stiffness found on AFM measurement of the nodules. (Fig. S1A–E). TFM revealed that the average cellular force was 125 Pa (range 21–349 Pa) (Fig. S2A,B), similar to previous reports of stromal cells (Muneevar et al., 2001; Morin et al., 2014). The range of force generation by myofibroblasts suggests great heterogeneity in this population, with some cells being highly contractile and others exerting far weaker force. Peak traction force was 634 Pa (range 93–2096 Pa), also showing a wide range with some cells able to produce a force of several kPa (Fig. S2A,B). Fully spread myofibroblasts were characterised by a distinctive distribution of cellular force (Fig. 2A,B), with oval, discrete force foci of high force magnitude, with the remaining cell area exerting a low force that was comparable to background noise levels in the gel (Fig. 2C; Fig. S3A,B).

A Live-cell confocal 2D TFM



B Myofibroblast force foci



C Force foci properties

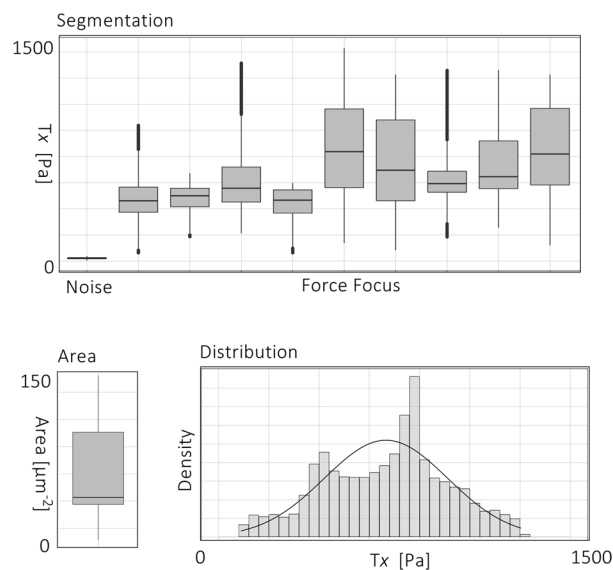


Fig. 2. Characterising the biophysical profile of myofibroblast force foci.

(A) Top two panels, confocal image of Calcein AM tagged myofibroblast (green) on 4.5 kPa PAA gel with marker beads (red) and corresponding traction stress heatmap showing localised areas of high traction force in red. Bottom panel, confocal image of immunofluorescence staining of F-actin of myofibroblast on 4.5 kPa hydrogel. (B) Traction stress plots showing localised areas of high traction force. Images represent single force foci from two myofibroblasts measured using traction force microscopy. Arrows signify vector fields of bead displacement used to track cellular forces. (C) Properties of force foci in human myofibroblasts. Box and whisker plots showing the area and range of forces in segmented force foci in human myofibroblasts with histogram showing the distribution of forces. $n=9$ force foci from three independent experiments.

Force foci in fully spread myofibroblasts varied in number, with most cells containing three to five. Their overall topography was highly conserved, with localised areas of high force magnitude adjacent to a more smooth distribution of lower force (Fig. 2C; Fig. S3A,B). Individual force foci were characterised by traction forces that followed a Gaussian distribution (Fig. 2C). Segmentation of the force foci confirmed that the remaining cell surface generated little force above background noise levels (Fig. 2C). Therefore, adhesion of myofibroblasts to the matrix is through these force foci and enables the application of traction force during remodelling. Together, these provide the first detailed subcellular measurements of force generation in human myofibroblasts on a substrate that reflects the *in vivo* mechanical environment. Notably, the topography and size of myofibroblast force foci ($8.1 \pm 3.3 \mu\text{m}$) mirrored the size of supermature focal complexes (suFA $8.5 \pm 3.6 \mu\text{m}$ to $9/9 \pm 3.1 \mu\text{m}$) previously described in myofibroblasts (Goffin et al., 2006) and corresponding fibrillar ECM proteins (Fig. 2B; Fig. S3A,B).

Traction forces are modulated during myofibroblast spreading

Next, we used single-cell force measurements to explore the spatiotemporal dynamics of myofibroblast force during cell spreading (Fig. 3A,B). We observed a distinct evolution of force profiles during spreading over time. On initial contact with the hydrogels, myofibroblasts were circular and traction forces localised to the cell periphery (Fig. 3A). Immunofluorescence staining of spreading myofibroblasts confirmed that these peripheral structures were characterised by dendritic actin networks with small, radially orientated F-actin stress fibres (Fig. 3C). When the cell was fully spread, cellular traction forces shifted to the discrete oval regions described previously (Fig. 3B). Segmentation of cellular forces at the cell periphery ($2 \mu\text{m}$ from cell edge) showed the remaining cell area exerted forces comparable to the background level (Fig. 3D). Comparing the traction force at early and late time points of cell spreading demonstrated that maximum and average traction forces remained constant, as did the area of traction forces above noise levels (Fig. 3E). Collectively, these results provide evidence for distinct biophysical profiles within myofibroblasts undergoing spreading, with maintenance of traction force during this process (Fig. 3E,F).

Distinct biophysical and cytoskeletal subpopulations in human myofibroblasts

Finally, we sought to investigate whether discrete biophysical subpopulations exist in human myofibroblasts. This is particularly important as force generation is a key aspect of the function of these cells. First, we quantified single-cell force profiles of human myofibroblasts ($n=59$ cells) during which hydrogel stiffness and imaging parameters were kept constant to facilitate comparison. Cell force profiles were normalised to cell area before input into principal component analysis (PCA) (Fig. 4A; Fig. S4A,B). Force profiles were created from meta-signatures of force measurements encompassing centiles of traction force and summary statistics for each cell. On inspection of the PCA plot, cells did not separate into obvious clusters (Fig. 4A; Fig. S4B). Instead, the PCA plot showed a small cluster of cells, with several more heterogeneous cell groups (Fig. 4A). PC1 captured the highest proportion of variance in the dataset (64.2%) and aligned cells based on their maximum and mean traction force without discrete clusters or subpopulations (Fig. S4A). Together, this suggests a continuum structure whereby myofibroblasts exist along a spectrum between high and low force-generating cells.

To identify potential clusters, we used unsupervised partitioning around medoids (PAM) clustering of the cells in principal component space with the parameter $k=3$ (Fig. 4D). Interestingly, each of the resulting clusters had distinct biophysical properties, with one composed of highly contractile cells. The second group exerted lower force, and there was a third intermediate population (Fig. 4D). Projecting the PAM clusters along the first principal component (PC) aligned each cluster with respect to maximum and mean traction force (Fig. 4E).

We then applied a separate computational workflow to resolve potential subpopulations. To partition single cells by their force profiles, we used an unsupervised clustering approach based on the Louvain algorithm, following recent approaches described for single-cell RNA-seq. For this, we plotted a k -nearest-neighbour (k -NN) graph for each pair of cells using the Euclidean distance between the scores of significant PCs to identify k -NNs (Fig. 4B,C). This graph was then refined to a shared nearest neighbour graph (SNN), informed by local neighbourhoods (Jaccard distance), and was then used as the input to the Louvain algorithm. Consistent with PCA projection, this method returned three biophysical clusters. Together, these data elucidate the presence of separate subpopulations of myofibroblasts with distinct biophysical properties, with a spectrum of high to low contractile cells existing simultaneously.

Finally, we integrated biophysical force measurements with morphological and cytoskeletal properties in myofibroblasts (Fig. 4F,G). For this, we performed immunofluorescence staining for F-actin on freshly isolated myofibroblasts on 4.5 KPa hydrogels, and at the same time point (60 min after seeding) we measured myofibroblast traction force. We quantified cell size, circularity, stress fibre length and orientation and used these metrics as an input for graph-based clustering. Remarkably, this again revealed three clusters with distinct cytoskeletal properties (Fig. 4F). One cluster was composed of large, polarized cells with highly organized and uniform stress fibres ('high' cluster). A second cluster was composed of intermediate size cells, with disorganized stress fibre length and orientation ('int' cluster). Finally, a third cluster was enriched for smaller cells exhibiting stress fibres with low orientation and length properties ('low' cluster) (Fig. 4F,G). Together, these show that topological cytoskeletal organization mirrors biophysical properties in myofibroblasts, with each composed of distinct subpopulations.

Conclusions

In summary, we have characterised the biophysical profile of primary human myofibroblasts isolated from a fibrotic microenvironment in unprecedented detail. Employing a combination of unsupervised computational analysis and single-cell traction force microscopy as functional readout we resolved the complex spatiotemporal pattern of myofibroblast force generation. Building a fibrotic model through nano-indentation of native Dupuytren's nodules enabled the first measurements of myofibroblast force generation in a representative mechanical environment. Focal complexes have previously been described in myofibroblasts (Goffin et al., 2006), but our results extend beyond this to illustrate the evolution and mechanics of these structures on binding collagen. During cell spreading the magnitude of traction forces remained stable, but their distribution was highly dynamic. On initial contact with the collagen-coated matrix, myofibroblasts exert traction force at the cell periphery that transforms to form force foci. It could be reasoned that this phenomenon facilitates an initial phase of cell-ECM interaction promoting cell spreading, followed by a second phase that permits binding to and remodelling of matrix proteins.

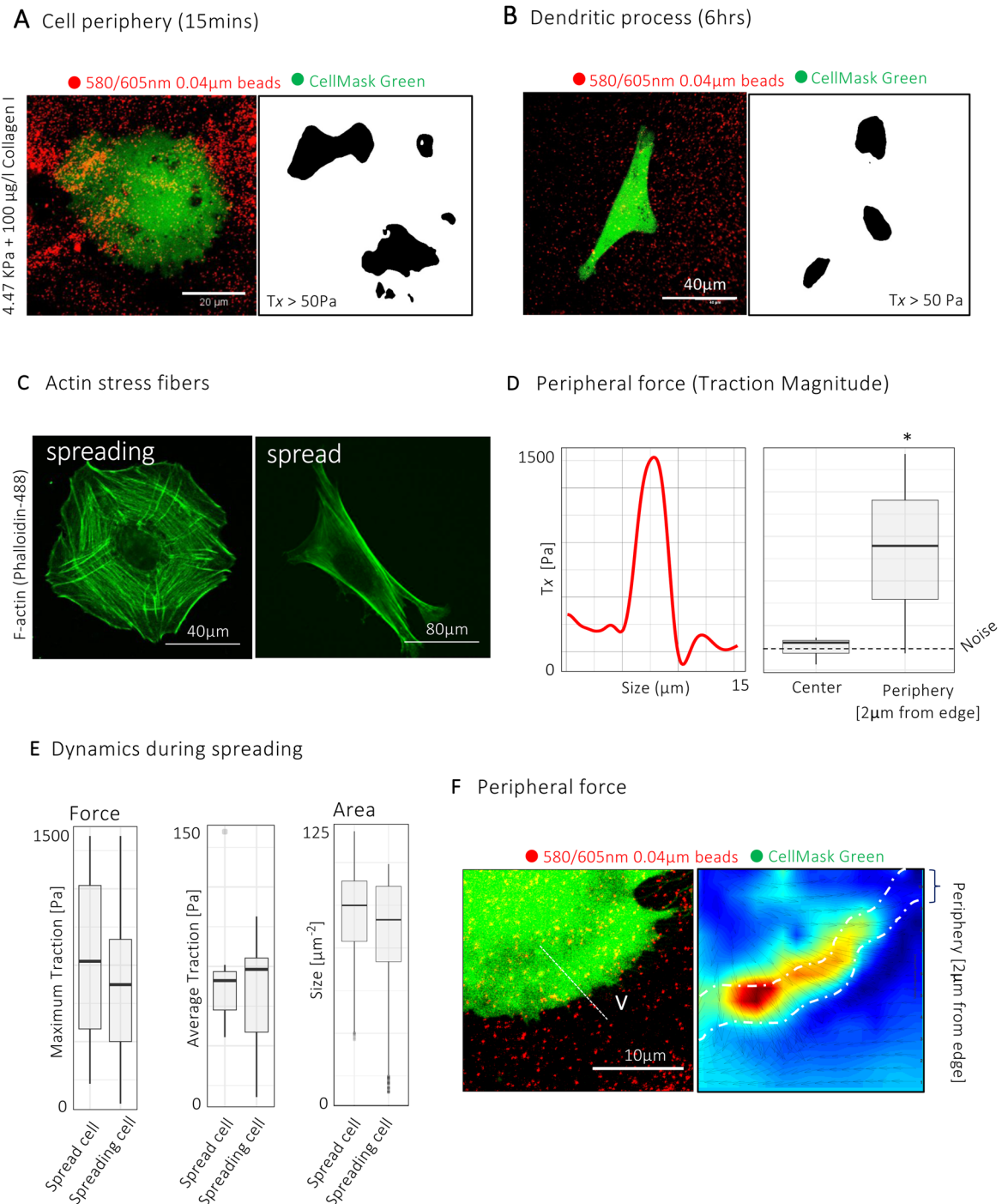


Fig. 3. Traction force is modulated during myfibroblast spreading. (A,B) Confocal images of Calcein-AM-tagged myfibroblasts (green) seeded on 4.5 kPa Polyacrylamide (PAA) hydrogel (A) 15 min and (B) 60 min after seeding, with corresponding binary plots of traction forces above noise level. Black regions represent areas of traction force above noise level (~ 50 Pa). T_x =Traction. (C) Confocal image of F-actin staining (Phalloidin-488) in spreading (15 min) and fully-spread myfibroblast (>60 min) showing organisation of F-actin and stress-fibre topology. (D) Line profile of traction-force magnitude across line V in F showing the distribution of force along one representative cell periphery and box and whisker plot showing mean traction force at cell periphery ($2 \mu\text{m}$ from cell edge) compared to the remaining cell surface (background) during spreading (15 min after seeding cells). $n=20$ myfibroblasts from three independent donors. $*P<0.05$ (Wilcoxon Rank Sum test). (E) Box and whisker plots showing maximum and mean traction forces, and area of traction force above noise levels in spreading and spread myfibroblasts. $n=12$ myfibroblasts from three independent experiments. (F) Confocal image of spreading myfibroblasts (green) and corresponding traction stress heatmap.

We also uncovered distinct biophysical subpopulations of myfibroblasts. These discrete subpopulations were placed along a linear trajectory following both PCA and graph-based clustering, supporting the concept of these cells as existing along a continuum. This may reflect an underlying differentiation path or could

represent a dynamic equilibrium within which cells flux between high and low contraction states.

Single-cell biology has uncovered many critical cellular processes, fostering a deep appreciation for the significance of heterogeneity in biology. To complement the quantification of biophysical profiles,

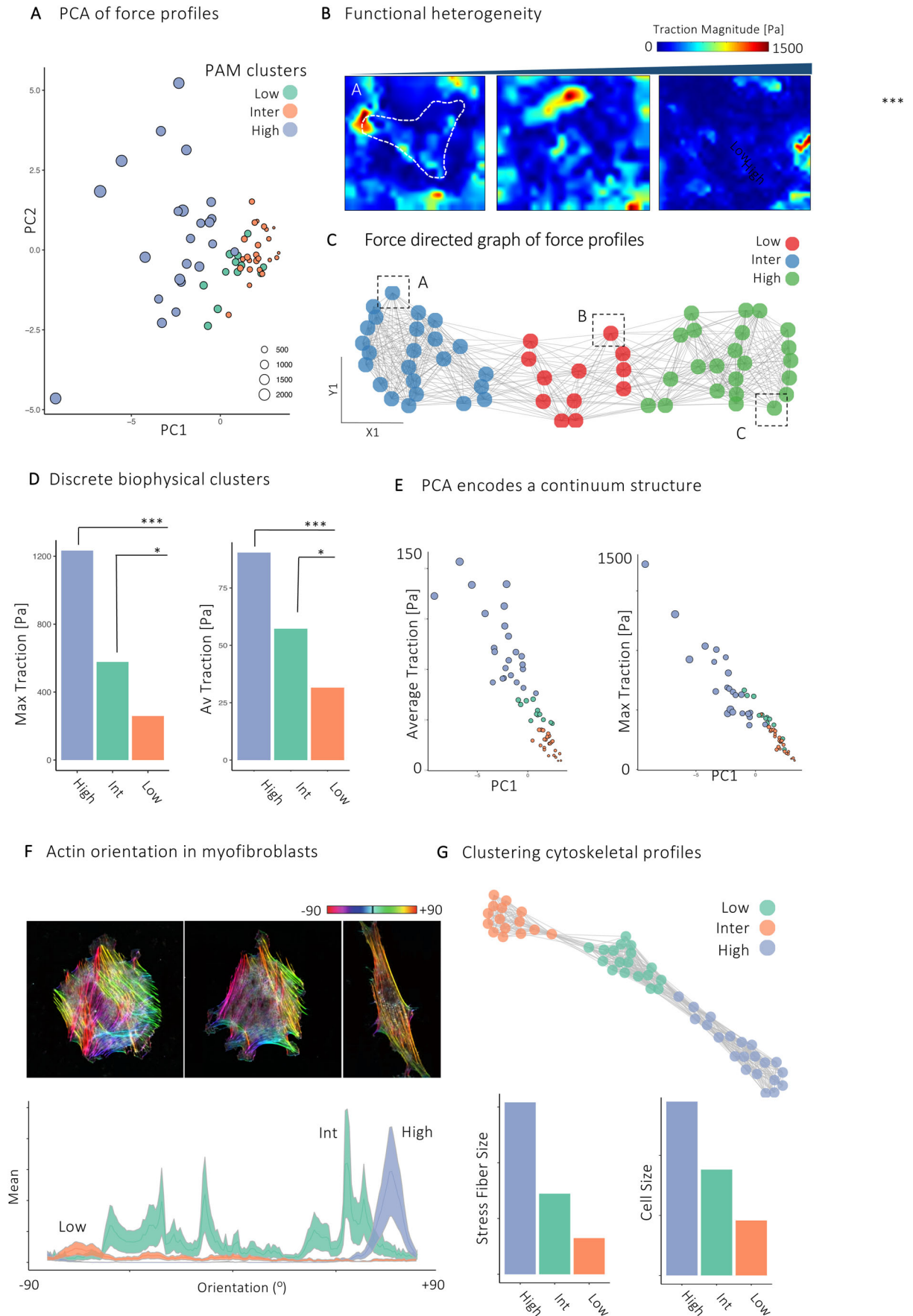


Fig. 4. See next page for legend.

Fig. 4. Distinct biophysical subpopulations of human myofibroblasts.

(A) Scatter plot projecting single-cell force profiles along the first two principal components (PC1 and PC2). Each point represents one cell and cells are coloured by PAM cluster ($n=59$ cells). (B) Corresponding traction force heatmaps of cells identified in dashed black squares in (C). (C) k -NN graph of PCA meta-signatures (force profiles) coloured by Louvain cluster. Each point represents a single cell ($n=59$ cells). (D) Bar plots of maximum and mean traction forces per PAM cluster. * P -value <0.05 and *** P -value <0.01 (Wilcoxon Rank Sum test, $n=59$ cells). (E) Scatter plot projecting maximum and average traction force per cell along the first principal component. Each point represents one cell and size represents maximum traction force ($n=59$, from >5 independent donors). (F) Immunofluorescence of actin orientation in representative myofibroblast types with corresponding quantification of actin stress fibre orientation ($n=59$ myofibroblasts from three independent experiments). (G) k -NN graph of myofibroblast cytoskeletal and morphological features (cell area, aspect ratio, stress-fibre length and stress-fibre orientation) with corresponding bar plots of stress-fibre length and cell size ($n=59$ myofibroblasts from three independent experiments). Scale bar: 20 μm .

we sought to integrate morphological and cytoskeletal parameters, and performed unsupervised clustering of myofibroblasts based on these properties. Although cell size and circularity did not directly influence traction forces in our experiment, we again noted three clear subpopulations. Indeed, cytoskeletal topology mirrored the biophysical profiles of myofibroblasts. Exploring the cytoskeletal clusters suggests that morphological heterogeneity was explained mostly by cell spreading and polarisation, with one large, highly polarised myofibroblast cluster, and two clusters of variable size with more disorganised actin organisation. This observation supports inferences made from our computational and experimental traction force analysis that suggest a unified continuum structure along which myofibroblasts transition between polarisation states. During this transition and cell spreading, large-scale modifications in traction force distribution and cytoskeletal structure were observed, but the magnitude of force generation remains stable. Moving forward, future work might also consider the time domain of this process.

Limitations of our study include the need for tissue digestion to isolate single cells, which likely exerts phenotypic effects on myofibroblasts. Also, although myofibroblasts are the predominant cell type in nodules, we performed no definitive enrichment step to isolate a pure myofibroblast population. With regards to the experimental protocol used, the necessity to obtain quantifiable bead displacements required the use of 4.5 kPa gels, which is the lower end of the force measurements in nodules. Looking forward, it would be important to integrate our single-cell biophysical and cytoskeletal profiling of myofibroblasts with other stromal cells to find potential conserved and distinct functional states. This would facilitate the development of detailed functional taxonomies of stromal cells in human disease. Our description of the biophysical readouts of primary human cells forms a foundation for future research that should aim to integrate functional parameters with gene expression and proteomic measurements to construct a validated cellular census of myofibroblasts.

MATERIALS AND METHODS**Patient samples**

After approval by the local ethical review committee (REC 07/H0706/81), tissue samples were obtained with informed consent from patients with DD. Dupuytren's nodular tissue was obtained from individuals with DD undergoing dermofasciectomy.

Cell culture

Cells from DD patients were isolated from α -SMA-rich nodules as described previously Verjee et al. (2009). Tissue samples were dissected into small

pieces and digested in DMEM (Lonza) with Type I collagenase (Worthington Biochemical Corporation) +DNase I (Roche Diagnostics) for up to 2 h at 37°C. Cells were cultured in DMEM with 5% (vol/vol) FBS and 1% penicillin-streptomycin at 37°C in a humidified incubator with 5% (vol/vol) CO₂. Cells before passage two were used for experiments.

Immunofluorescence and confocal microscopy

Dupuytren's myofibroblasts were fixed with 4% paraformaldehyde in PBS for 20 min, longitudinally bisected, embedded in paraffin wax, and 7- μm sections from the cut surface were processed for immunofluorescence. The tissue sections were stained with Phalloidin-AF488 (Life Technologies). Nuclei were counterstained with DAPI (4, 6-diamidino-2-phenylindole; Sigma-Aldrich) and mounted using Prolong™ Gold anti-fade (Life Technologies). Fluorescent images were captured using a confocal system (Zeiss LSM 710).

F-actin orientation analysis

The orientation properties of the actin filaments in myofibroblast immunofluorescence images (Phalloidin-488) were computed based on the evaluation of the structure tensor in a local neighbourhood using the Java plugin for ImageJ (<http://imagej.nih.gov/>) 'OrientationJ'. After specifying the size of a Gaussian-shaped window, the program computes the structure tensor for each pixel in the image by sliding the Gaussian analysis window over the entire image. The local orientation properties are computed and are then visualised as gray-level or colour images with the orientation being typically encoded in colour. The data presentation was performed using the 'ggplot2' R package (R Version 3.5.). We analysed the F-actin orientations from at least 60 individual cells over the course of at least three independent experiments.

Atomic force microscopy

Mechanical measurements were obtained using an Asylum Research MFP-3D atomic force microscope (Oxford Instruments). Fresh tissue samples from DD patients were dissected to obtain an approximately 10 μm cube from the centre of the nodule. This was then embedded in OCT and snap frozen in liquid nitrogen. Using a cryostat, 30 μm longitudinal slices were cut and mounted onto a glass slide. Tissue stiffness was measured through micro-indentation using a 0.072 Nm⁻¹ probe with spherical 5 μm SiO₂ tip (NovaScan) and the cantilever spring constant was calibrated using the thermal fluctuation method. 100 nano-indentation measurements were taken from 10 \times 10 μm squares, with at least three squares per nodule, with the sample in double-distilled water at room temperature. Elastic modulus was calculated using the Hertz model from indentation profiles using MFP-3D software (Oxford Instruments and Igor).

Preparation of polyacrylamide hydrogels

Polyacrylamide (PAA) gels were prepared as previously described in Colin-York et al. (2017). Briefly, 4.5 kPa polyacrylamide gels were prepared by combining acrylamide monomers (Sigma-Aldrich) at 10% and bis-acrylamide cross-linkers (Sigma-Aldrich). Polymerization was initiated by the addition of TEMED (Sigma-Aldrich) followed by 10% Ammonium persulfate (Sigma-Aldrich) at a volume ratio of 1:250 and 1:100, respectively. The gel solution was pipetted between two glass coverslips, one of which had been treated with APTMS 0.5% (Sigma-Aldrich) followed by 0.5% glutaraldehyde (Sigma-Aldrich) to firmly attach the gel to the coverslip.

PAA functionalization was achieved using the ultraviolet (UV) activated cross-linker Sulfo-SANPAH (Thermo Fisher Scientific). Each gel was coated with 20 mg per ml solution of Sulfo-SANPAH and exposed to 365 nm UV light for 10 min. The gel was then washed to remove any excess cross-linker and then coated with a 100 $\mu\text{g}/\text{ml}$ Type I Collagen (First Link) and incubated at 37°C for 1 h. Gels were then washed and incubated at 37°C before cell seeding.

Traction force microscopy

Live cell imaging was performed at 37°C in Phenol-Red-free DMEM (Gibco 2106309) without serum. Images were acquired using an inverted wide-field confocal microscope (Zeiss LSM 710) fitted with a stage

incubator (5% CO₂ in air, 37°C). Images of fluorescent beads (fiducial markers) were acquired in the Texas Red channel (580/605 nm) and cells acquired in the Alexa-Fluor 488 channel (488 nm). Imaging was performed using a 63× (1.4 NA) oil objective and images were processed using ImageJ software. Average pixel size was 153.3 nm. Cells were removed from the gel surface using Trypsin (0.5%) after 60 min.

Data processing was performed as described in Colin-York et al. (2017) using ImageJ plugins. First, images were imported into ImageJ using Bioformats and corrected for experimental drift between each image using a template-matching and slice-alignment plugin. A normalised correlation-coefficient-matching method was implemented with subpixel registration. Following this, particle image velocimetry (PIV) was applied to quantify bead displacements using a cross-correlation algorithm with an iterative window size of 64 pixels and 32 pixels yielding displacement vectors of 16 pixels and a final resolution of 2.4 μm. Post-processing of PIV vectors was undertaken using a normalised median test (noise level of 0.2 and threshold of 5.0) to filter and replace erroneous displacement vectors with the median value from nearby vectors ($n=30$). This process compares each vector with its 30 nearest neighbours and corrects for inaccurate displacement vectors that result from noise in the raw images.

Fourier transform traction cytometry (FTTC) was used to reconstruct traction forces from displacements fields. The parameters used in the FTTC code included a pixel size of 0.153 μm, Poisson's ratio of 0.5 and the elastic modulus of the gel was 4.5 kPa. A gel stiffness of 4.5 KPa was used to obtain quantifiable bead displacements. The appropriate regularisation factor λ was determined empirically as per Schiller et al., 2013. This value was selected to minimise the contribution of noise and optimise traction force recovery from raw image sequences. A value of $1e^{-10}$ was selected and kept constant throughout all experiments.

Computational analysis

Feature selection and dimensional reduction

Downstream analysis and visualisation were performed using MATLAB (Mathworks) and R (R Version 3.5). We first constructed meta-signatures for single-cell force profiles using percentiles and summary statistics (mean, max, median and standard error) and normalised these to cell area. Next, normalised force profiles were centred and scaled before input to principal component analysis, implemented using the 'prcomp' function from the 'stats' R package. To initially partition cells, we used unsupervised PAM clustering of the cells in principal component space with the parameter $k=3$.

k-NN-graph-based clustering

After PCA, significant principal components were identified using the permutation test implemented using the 'permutationPA' function from the 'jackstraw' R package. This test identified seven significant PCs and these were used as input for graph-based clustering. To cluster single cells by their force profiles, we used unsupervised clustering based on the Louvain community-detection algorithm. For this, we first constructed a k -NN graph using, for each pair of cells, the Euclidean distance between the scores of significant principal components as the metric. The k -NN graph was computed using the function 'nng' from the R package 'cccd'. After this, the k -NN graph was refined using the shared local neighbourhoods of points (Jaccard Distance) and clustered using the 'louvain_cluster' function from the 'igraph' R package.

Acknowledgements

We are grateful to our clinical collaborators Christopher Bainbridge, David Warwick, Lorraine Harry and Dominique Davidson for provision of tissue samples from their patients. We thank the Imaging Centre at the Kennedy Institute of Rheumatology for their support in microscopy.

Competing interests

The authors declare no competing or financial interests.

Author contributions

Conceptualization: T.B.L., M. Feldmann, W.X., M. Fritzsche, J.N.; Methodology: T.B.L., H.C.-Y., M.C., C.B., M. Fritzsche, J.N.; Formal analysis: T.B.L., C.B.; Investigation: T.B.L., F.E.M., M. Fritzsche; Resources: H.C.-Y., J.N.; Writing -

original draft: T.B.L.; Writing - review & editing: L.W., H.C.-Y., F.E.M., M.C., M. F., W.X., D.F., J.N.; Supervision: H.C.-Y., F.E.M., C.B., M. Fritzsche, D.F.; Project administration: L.W., J.N.; Funding acquisition: M. Feldmann, W.X., J.N.

Funding

This work was funded by the Royal College of Surgeons of England, the Kennedy Institute of Rheumatology Studentship [MSP 13 14 11] and the Oxford-Celgene Research Fellowship [grant no. AZR00610].

Supplementary information

Supplementary information available online at <http://bio.biologists.org/lookup/doi/10.1242/bio.049809.supplemental>

References

- Aizarani, N., Saviano, A., Sagar, M., Maily, L., Durand, S., Herman, J. S., Pessaux, P., Baumert, T. F. and Grün, D. (2019). A human liver cell atlas reveals heterogeneity and epithelial progenitors. *Nature* **572**, 199-204. doi:10.1038/s41586-019-1373-2
- Badalamente, M. A., Stern, L. and Hurst, L. C. (1983). The pathogenesis of Dupuytren's contracture: contractile mechanisms of the myofibroblasts. *J. Hand Surg.* **8**, 235-243. doi:10.1016/S0363-5023(83)80150-6
- Colin-York, H., Shrestha, D., Felce, J. H., Waithe, D., Moeendarbary, E., Davis, S. J., Eggeling, C. and Fritzsche, M. (2016). Super-Resolved Traction Force Microscopy (STFM). *Nano Lett.* **16**, 2633-2638. doi:10.1021/acs.nanolett.6b00273
- Colin-York, H., Eggeling, C. and Fritzsche, M. (2017). Dissection of mechanical force in living cells by super-resolved traction force microscopy. *Nat. Protoc.* **12**, 783-796. doi:10.1038/nprot.2017.009
- Colin-York, H., Javanmardi, Y., Barbieri, L., Li, D., Korobchevskaya, K., Guo, Y., Hall, C., Taylor, A., Khuon, S., Sheridan, G. K. et al. (2019a). Spatiotemporally super-resolved volumetric traction force microscopy. *Nano Lett.* **19**, 4427-4434. doi:10.1021/acs.nanolett.9b01196
- Colin-York, H., Javanmardi, Y., Skamrahl, M., Kumari, S., Chang, V. T., Khuon, S., Taylor, A., Chew, T.-L., Betzig, E., Moeendarbary, E. et al. (2019b). Cytoskeletal control of antigen-dependent T cell activation. *Cell Rep.* **26**, 3369-3379. doi:10.1016/j.celrep.2019.02.074
- Giustacchini, A., Thongjuea, S., Barkas, N., Woll, P. S., Povinelli, B. J., Booth, C. A. G., Sopp, P., Norfo, R., Rodriguez-Meira, A., Ashley, N. et al. (2017). Single-cell transcriptomics uncovers distinct molecular signatures of stem cells in chronic myeloid leukemia. *Nat. Med.* **23**, 692-702. doi:10.1038/nm.4336
- Goffin, J. M., Pittet, P., Csucs, G., Lussi, J. W., Meister, J.-J. and Hinz, B. (2006). Focal adhesion size controls tension-dependent recruitment of α -smooth muscle actin to stress fibers. *J. Cell Biol.* **172**, 259-268. doi:10.1083/jcb.200506179
- Hinz, B. and Gabbiani, G. (2003). Mechanisms of force generation and transmission by myofibroblasts. *Curr. Opin. Biotechnol.* **14**, 538-546. doi:10.1016/j.copbio.2003.08.006
- Hinz, B., Celetta, G., Tomasek, J. J., Gabbiani, G. and Chaponnier, C. (2001). Alpha-smooth muscle actin expression upregulates fibroblast contractile activity. *Mol. Biol. Cell* **12**, 2730-2741. doi:10.1091/mbc.12.9.2730
- Karki, P. and Birukova, A. A. (2018). Substrate stiffness-dependent exacerbation of endothelial permeability and inflammation: mechanisms and potential implications in ALI and PH (2017 Grover Conference Series). *Pulmon. Circ.* **8**, 2045894018773044. doi:10.1177/2045894018773044
- Kinchen, J., Chen, H. H., Parikh, K., Antanaviciute, A., Jagielowicz, M., Fawcner-Corbett, D., Ashley, N., Cubitt, L., Mellado-Gomez, E., Attar, M. et al. (2018). Structural remodeling of the human colonic mesenchyme in inflammatory bowel disease. *Cell* **175**, 372-386. doi:10.1016/j.cell.2018.08.067
- Liu, F. and Tschumperlin, D. J. (2011). Micro-mechanical characterization of lung tissue using atomic force microscopy. *J. Vis. Exp.*, e2911. doi:10.3791/2911
- Liu, F., Lagares, D., Choi, K. M., Stopfer, L., Marinković, A., Vrbanc, V., Probst, C. K., Hiemer, S. E., Sisson, T. H., Horowitz, J. C. et al. (2015). Mechanosignaling through YAP and TAZ drives fibroblast activation and fibrosis. *Am. J. Physiol. Lung Cell. Mol. Physiol.* **308**, L344-L357. doi:10.1152/ajplung.00300.2014
- Liu, F., Haeger, C. M., Dieffenbach, P. B., Sicard, D., Chrobak, I., Coronata, A. M., Suárez Velandia, M. M., Vitali, S., Colas, R. A., Norris, P. C. et al. (2016). Distal vessel stiffening is an early and pivotal mechanobiological regulator of vascular remodeling and pulmonary hypertension. *JCI Insight* **1**, e86987. doi:10.1172/jci.insight.86987
- Marinković, A., Mih, J. D., Park, J.-A., Liu, F. and Tschumperlin, D. J. (2012). Improved throughput traction microscopy reveals pivotal role for matrix stiffness in fibroblast contractility and TGF- β responsiveness. *Am. J. Physiol. Lung Cell. Mol. Physiol.* **303**, L169-L180. doi:10.1152/ajplung.00108.2012
- Morin, T. R., Jr, Ghassem-Zadeh, S. A. and Lee, J. (2014). Traction force microscopy in rapidly moving cells reveals separate roles for ROCK and MLCK in the mechanics of retraction. *Exp. Cell Res.* **326**, 280-294. doi:10.1016/j.yexcr.2014.04.015

- Munevar, S., Wang, Y.-L. and Dembo, M. (2001). Traction force microscopy of migrating normal and H-ras transformed 3T3 fibroblasts. *Biophys. J.* **80**, 1744-1757. doi:10.1016/S0006-3495(01)76145-0
- Polacheck, W. J. and Chen, C. S. (2016). Measuring cell-generated forces: a guide to the available tools. *Nat. Methods* **13**, 415-423. doi:10.1038/nmeth.3834
- Rayan, G. M., Parizi, M. and Tomasek, J. J. (1996). Pharmacologic regulation of Dupuytren's fibroblast contraction in vitro. *J. Hand Surg. [Am.]* **21**, 1065-1070. doi:10.1016/S0363-5023(96)80317-0
- Schiller, H. B., Hermann, M.-R., Polleux, J., Vignaud, T., Zanivan, S., Friedel, C. C., Sun, Z., Raducanu, A., Gottschalk, K.-E., Théry, M. et al. (2013). β 1- and α v-class integrins cooperate to regulate myosin II during rigidity sensing of fibronectin-based microenvironments. *Nat. Cell Biol.* **15**, 625-636. doi:10.1038/ncb2747
- Tseng, Q., Wang, I., Duchemin-Pelletier, E., Azioune, A., Carpi, N., Gao, J., Filhol, O., Piel, M., Théry, M. and Balland, M. (2011). A new micropatterning method of soft substrates reveals that different tumorigenic signals can promote or reduce cell contraction levels. *Lab. Chip* **11**, 2231-2240. doi:10.1039/c0lc00641f
- Van Beuge, M. M., Ten Dam, E.-J. P. M., Werker, P. M. N. and Bank, R. A. (2016). Matrix and cell phenotype differences in Dupuytren's disease. *Fibrogenesis Tissue Repair* **9**, 9. doi:10.1186/s13069-016-0046-0
- Verjee, L. S., Midwood, K., Davidson, D., Essex, D., Sandison, A. and Nanchahal, J. (2009). Myofibroblast distribution in Dupuytren's cords: correlation with digital contracture. *J. Hand Surg.* **34**, 1785-1794. doi:10.1016/j.jhsa.2009.08.005
- Verjee, L. S., Midwood, K., Davidson, D., Eastwood, M. and Nanchahal, J. (2010). Post-transcriptional regulation of α -smooth muscle actin determines the contractile phenotype of Dupuytren's nodular cells. *J. Cell. Physiol.* **224**, 681-690. doi:10.1002/jcp.22167
- Verjee, L. S., Verhoekx, J. S. N., Chan, J. K. K., Krausgruber, T., Nicolaidou, V., Izadi, D., Davidson, D., Feldmann, M., Midwood, K. S. and Nanchahal, J. (2013). Unraveling the signaling pathways promoting fibrosis in Dupuytren's disease reveals TNF as a therapeutic target. *Proc. Natl Acad. Sci. USA* **110**, E928-E937. doi:10.1073/pnas.1301100110
- Villani, A.-C., Satija, R., Reynolds, G., Sarkizova, S., Shekhar, K., Fletcher, J., Griesbeck, M., Butler, A., Zheng, S., Lazo, S. et al. (2017). Single-cell RNA-seq reveals new types of human blood dendritic cells, monocytes, and progenitors. *Science* **356**, eaah4573. doi:10.1126/science.aah4573
- Wang, J., Chen, H., Seth, A. and Mcculloch, C. A. (2003). Mechanical force regulation of myofibroblast differentiation in cardiac fibroblasts. *Am. J. Physiol. Heart Circ. Physiol.* **285**, H1871-H1881. doi:10.1152/ajpheart.00387.2003
- Wynn, T. A. and Ramalingam, T. R. (2012). Mechanisms of fibrosis: therapeutic translation for fibrotic disease. *Nat. Med.* **18**, 1028-1040. doi:10.1038/nm.2807

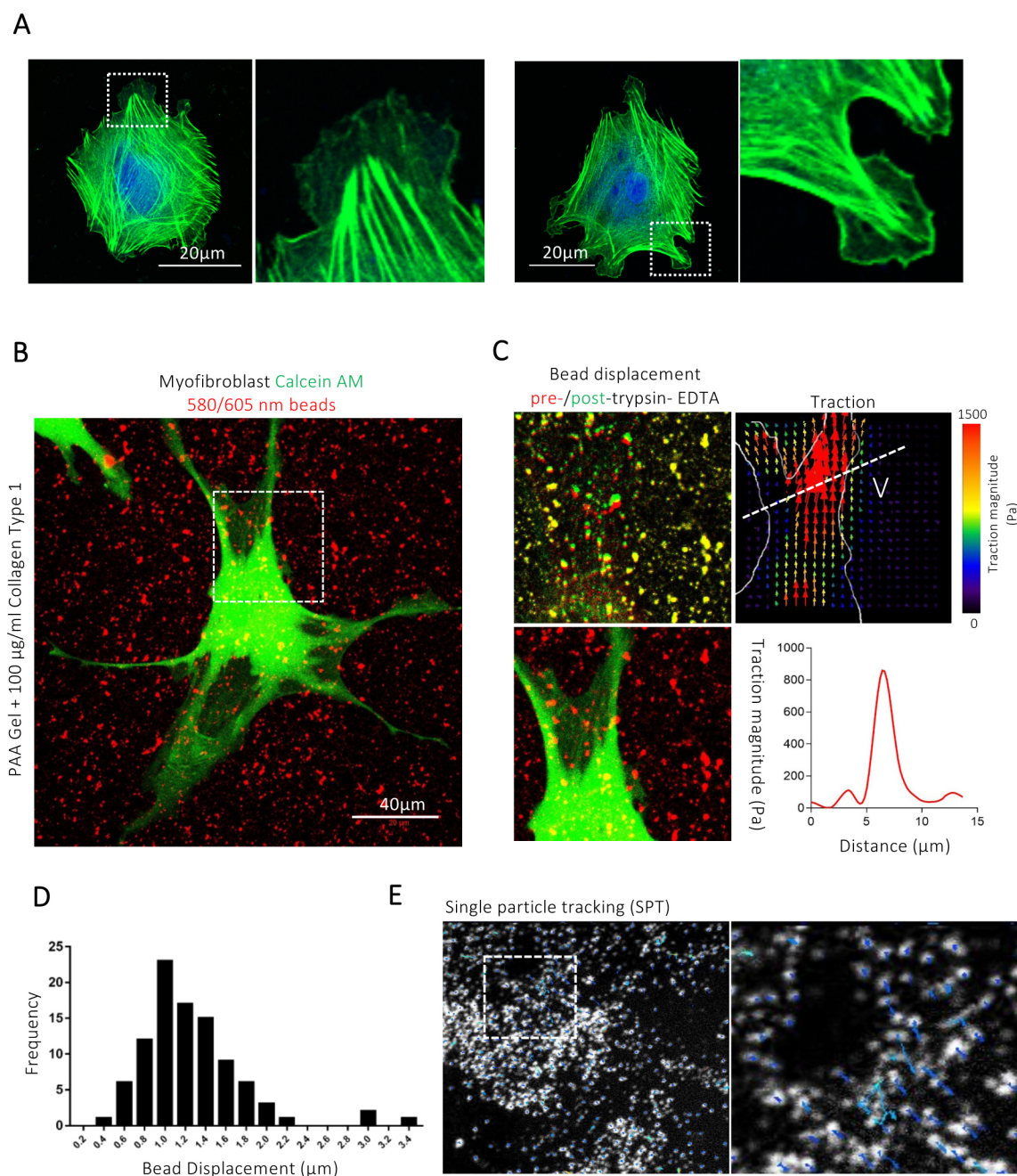


Fig S1. Experimental and computational setup for high resolution TFM

A) Confocal images of DD myofibroblasts on the surface of 4.5kPa hydrogel stained with Phalloidin-AF488 (Green) labelling F-actin. Cells were seeded on hydrogels 60 minutes prior to staining to confirm stress fibre formation on softer environments. Right panels are zoomed regions highlighted by white dashed squares. B) Confocal image of myofibroblast tagged with Calcein AM (green) on 4.5kPa PAA gel with fluorescent beads (red) on the surface. C) Image analysis workflow of traction force microscopy (TFM). Top left, confocal image from white square in (B) demonstrating bead displacement on gel surface before and after addition of trypsin. Top right, corresponding force vector plot. Bottom left, confocal image of myofibroblasts from white dashed square in Figure 1B. Bottom right, line profile of Line V in (B) showing linear profile of peak traction force generation from one human myofibroblast. D) Histogram of bead displacements from > 50 cells from three independent experiments with cells seeded on to 4.5KPa hydrogels. E) Single particle tracking (SPT) of fiducial markers on PAA gel surface. Magnification x63. White points represent beads and tracks signify movement after removing cell from gel surface.

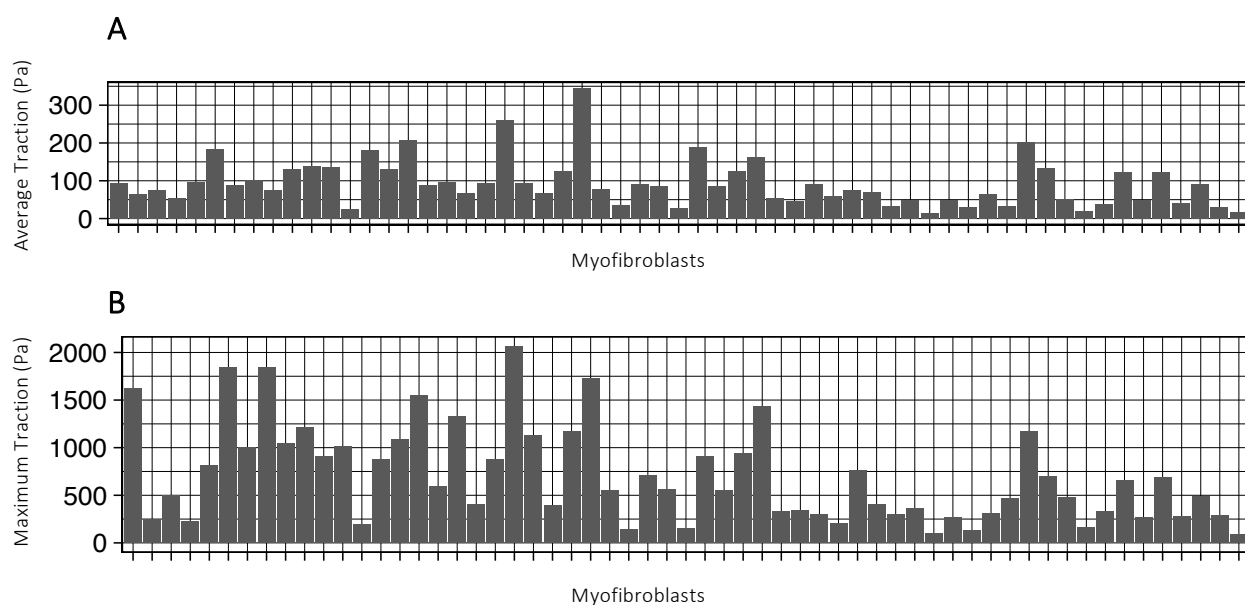


Fig S2. Cellular traction forces of human myofibroblasts.

A-B) Bar plots demonstrating average normalized (A) and peak (B) traction force in myofibroblasts on 4.5kPa PAA hydrogels ($n = 46$ cells from >10 independent donors). X axis represents individual myofibroblasts. Pa = Pascal.

A High resolution profiling of myfibroblast force generation

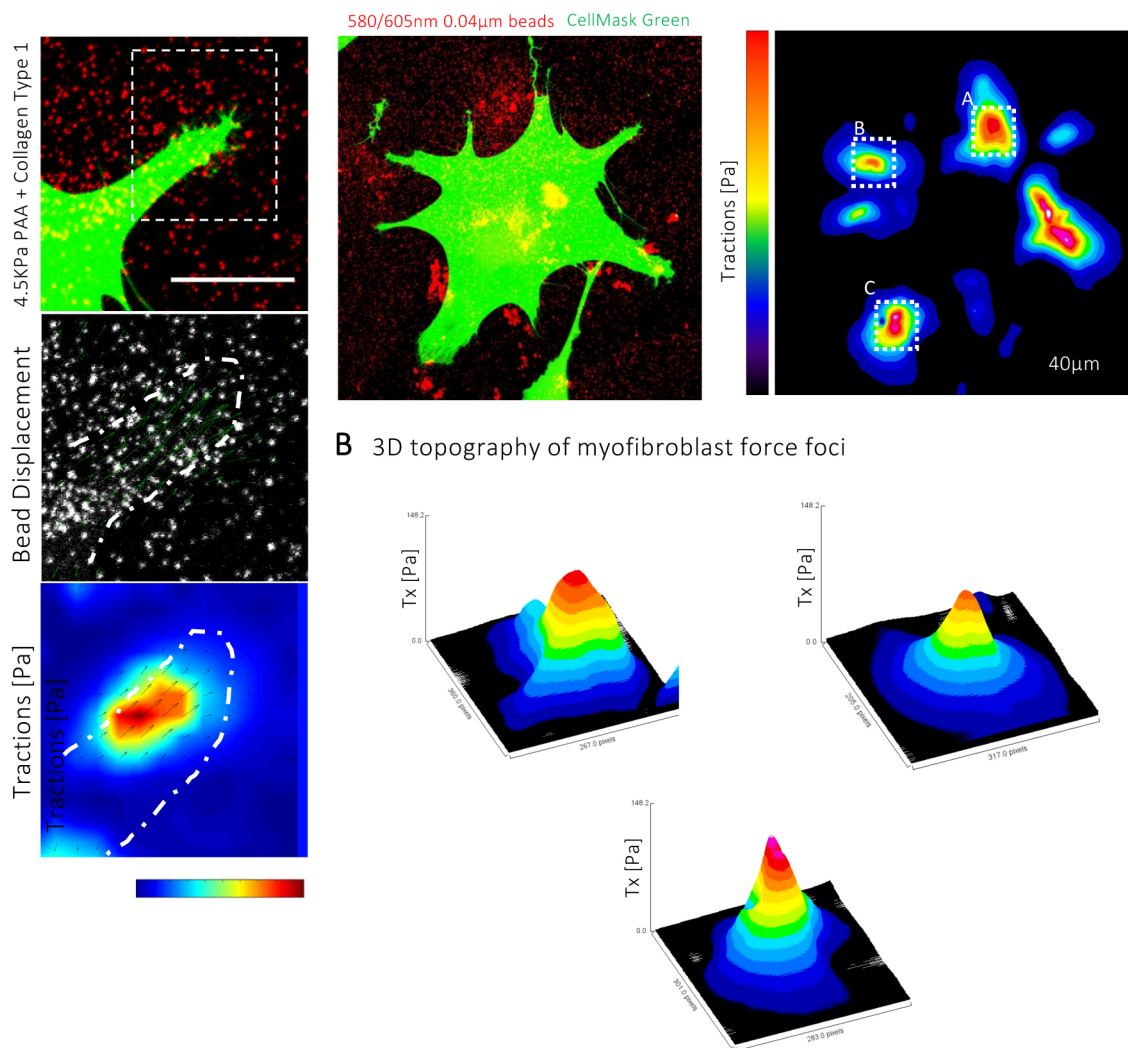
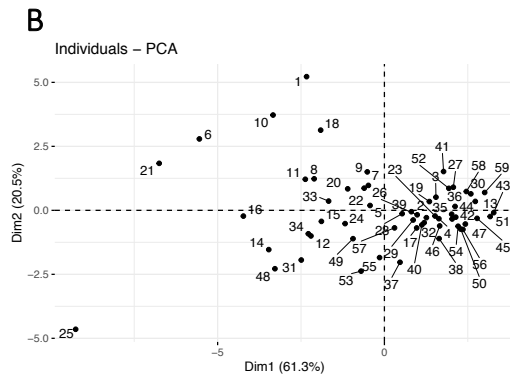
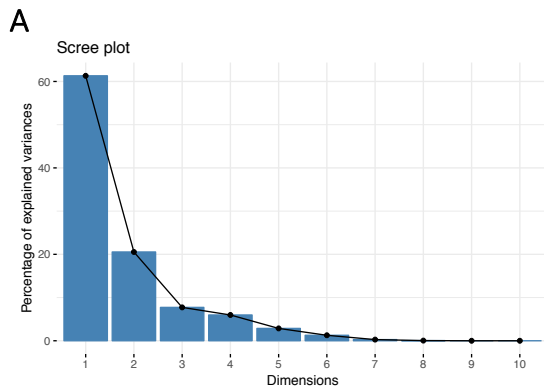


Fig S3. Myfibroblast traction forces are discrete and localized.

A) Traction stress heatmap and corresponding confocal image of Calcein AM tagged myfibroblast (Green) on 4.5 kPa PAA gel with marker beads (Red) showing localized area of high traction force in red. B) 3D surface plots of regions indicated by three white lines in (A).



C

	0Quantile 1	Quantile 2	Quantile 2	Quantile 4	Mean	Max	Min	Median
-73.949	16.511	37.438	88.196	1627.742	94.08010284	1627.742	-73.949	37.438
0.188	35.3585	50.74	79.088	246.718	64.4955709	246.718	0.188	50.74
-8.78	14.676	29.175	100.238	501.704	74.87926362	501.704	-8.78	29.175
3.404	27.246	46.2035	77.001	224.089	55.49664636	224.089	3.404	46.2035
-3.998	34.647	62.007	117.774	817.476	95.58946676	817.476	-3.998	62.007
-70.163	62.56275	115.0595	220.842	1838.217	184.8466745	1838.217	-70.163	115.0595
-12.92	26.022	51.427	108.9345	1003.883	88.03194957	1003.883	-12.92	51.427
-13.822	33.569	63.29	123.352	1845.207	100.9565914	1845.207	-13.822	63.29
-21.027	26.431	48.174	91.267	1048.177	74.42248851	1048.177	-21.027	48.174
-71.897	39.31675	80.8835	171.86925	1211.963	131.1515944	1211.963	-71.897	80.8835
-37.907	35.822	92.1645	197.32625	913.714	137.7150864	913.714	-37.907	92.1645
-2.581	56.502	110.495	165.681	1013.564	135.6739786	1013.564	-2.581	110.495
0.423	10.2305	18.068	33.475	196.014	26.162897	196.014	0.423	18.068
-11.113	81.105	135.235	219.982	871.862	180.8450832	871.862	-11.113	135.235
-6.613	52.7185	85.0335	167.493	1090.56	130.3096729	1090.56	-6.613	85.0335
-21.131	46.7495	125.356	256.2575	1554.105	207.2889641	1554.105	-21.131	125.356
-0.247	30.676	52.118	101.316	593.399	87.35433952	593.399	-0.247	52.118
-54.857	25.828	55.294	105.39025	1329.1	96.29688204	1329.1	-54.857	55.294
-9.882	17.405	36.98	89.893	401.344	66.24065976	401.344	-9.882	36.98
-16.115	43.821	71.351	116.669	872.241	94.35488568	872.241	-16.115	71.351
-65.143	54.98	125.433	356.497	2067.478	260.7961501	2067.478	-65.143	125.433
-14.379	24.362	47.1765	119.475	1130.176	93.59135519	1130.176	-14.379	47.1765
-1.643	19.885	36.863	90.003	396.879	66.38333143	396.879	-1.643	36.863
1.344	32.795	61.019	197.8635	1172.052	125.6989447	1172.052	1.344	61.019
-5.879	131.0705	260.259	459.09	1727.203	344.8636953	1727.203	-5.879	260.259
-11.997	19.38525	55.2185	103.543	549.461	77.8732799	549.461	-11.997	55.2185
-20.615	15.808	25.706	49.534	143.72	34.47582742	143.72	-20.615	25.706
-14.078	30.709	49.311	112.414	704.702	91.48031991	704.702	-14.078	49.311
-10.77	22.663	52.672	125.7995	557.303	85.91640882	557.303	-10.77	52.672
-0.45	12.375	21.66	35.71025	147.945	26.96299115	147.945	-0.45	21.66
1.834	25.219	129.842	281.052	908.756	188.5235953	908.756	1.834	129.842
-6.426	19.811	42.63	124.263	555.155	84.6542758	555.155	-6.426	42.63
-25.391	42.233	77.002	161.474	942.072	124.9798771	942.072	-25.391	77.002
-0.421	38.8225	80.1485	227.60475	1430.395	162.1959635	1430.395	-0.421	80.1485
-3.051	15.357	28.4555	63.279	333.604	53.32546786	333.604	-3.051	28.4555
-6.804	13.9835	24.2	48.9035	340.872	46.47724549	340.872	-6.804	24.2
7.033	51.23225	77.628	121.3845	294.6	92.41150286	294.6	7.033	77.628
2.801	27.389	52.227	84.321	204.228	59.25361872	204.228	2.801	52.227
-0.879	21.554	35.304	71.018	764.737	75.67327553	764.737	-0.879	35.304
-5.947	24.85375	50.338	98.65825	401.037	71.38030113	401.037	-5.947	50.338
-18.287	16.484	27.084	40.971	303.583	33.31712864	303.583	-18.287	27.084
-1.6	15.873	29.91	62.88	363.333	48.56106402	363.333	-1.6	29.91
0.309	6.99375	10.747	18.508	96.291	15.13409987	96.291	0.309	10.747
-4.478	15.3015	28.04	66.8585	264.586	47.69786395	264.586	-4.478	28.04
-1.205	12.85525	21.0225	37.96425	129.336	30.13667467	129.336	-1.205	21.0225
-3.9	20.087	42.172	76.75	306.733	64.62686512	306.733	-3.9	42.172
-1.227	15.495	27.5505	46.37775	463.838	33.64296456	463.838	-1.227	27.5505
-0.446	46.493	129.329	289.816	1174.672	201.4557806	1174.672	-0.446	129.329
-20.873	45.772	91.688	170.936	696.612	133.0535466	696.612	-20.873	91.688
0.007	14.54875	28.3315	60.94325	475.047	51.56099115	475.047	0.007	28.3315
0.444	7.4195	11.571	19.4375	164.98	19.19321317	164.98	0.444	11.571
-6.605	16.951	28.334	43.607	331.359	37.88496623	331.359	-6.605	28.334
-2.253	51.834	103.293	174.0505	652.082	124.1927785	652.082	-2.253	103.293
-1.93	16.854	28.7775	63.69675	264.938	48.39036521	264.938	-1.93	28.7775
-4.02	40.277	77.922	166.701	689.094	122.8483949	689.094	-4.02	77.922
0.769	17.88075	28.4095	47.81075	279.397	41.52593367	279.397	0.769	28.4095
-3.381	39.90125	76.7955	123.13925	491.334	90.85562532	491.334	-3.381	76.7955
-1.128	11.383	18.688	32.672	288.166	30.33645792	288.166	-1.128	18.688
-0.005	7.611	13.657	23.119	94.021	18.04378415	94.021	-0.005	13.657

Fig S4. Principal component analysis of human myofibroblast force signatures.

A) Bar plot with overlay of line plot (Scree plot) showing variance explained by each principal component in single cell force profiles. Dimensions is principal components. B) Scatter plot projecting single cell force profiles along the first two principal components (Dim1 and Dim2). Each point represents one cell, and each is labelled by the order in which it was collected ($n = 59$, from >5 independent donors). C) Summary statistics for clustering.